VIP **Zinc-Ion Batteries** | *Very Important Paper*

Multisite Cooperative Regulation of Solvation and Interface via Dynamic Additive Engineering for Highly Reversible Zinc Batteries

Mengke Su, Haozhen Dou,* Jinliang Yan, Sitong Liu, Mi Xu, Chuangwei Liu, Xin Wang,* and Zhongwei Chen*

Abstract: Inexhaustible additives have been reported to enhance the reversibility of aqueous zinc-ion batteries (AZIBs). However, the structure–performance relationship of additive molecules remains elusive, particularly regarding multisite coordination-mediated synergistic regulation of solvation and interface. Herein, a dynamic configuration reconstruction mechanism that orchestrates the multisite regulation of solvation and interface is unveiled by utilizing a series of polyhydroxy additive prototypes, demonstrating that the increase of functional groups and chain flexibility in multifunctional-group molecules (MGMs) contributes to boosting battery performance. MGM with folded configuration engages in multisite Zn^{2+} coordination in the solvation shell, effectively minimizing active H_2O molecule to suppress parasitic reactions, while its configuration transition to straight-chain architecture enables multisite parallel adsorption on Zn anode interface, thus accelerating desolvation kinetics and steering (002)-facet-dominated Zn deposition. Remarkably, Zn//Zn cells achieve long cycle life of 7000 h and subzero-temperature operation, and Zn//PANI pouch cell maintains nearly 100% capacity retention after 500 cycles. This work opens a fascinating avenue for developing high-performance batteries via dynamic additive engineering.

Introduction

Aqueous zinc-ion batteries (AZIBs) are considered as one of the most promising next-generation energy storage devices for large-scale energy storage applications due to their attributes of intrinsic safety and low cost of aqueous electrolytes, as well as high abundance, high volumetric capacity (5855 mAh cm^{-3}), and low redox potential (-0.762 V versus SHE) of Zn metal anode.[1] In mild aqueous electrolytes, H_2O molecule in the Zn^{2+} solvation shell of $[Zn(H_2O)_6]^{2+}$ exhibits high chemical reactivity, which induces hydrogen evolution reaction (HER) and local pH elevation, followed by the chemical corrosion with the formation of by-production ($Zn_4SO_4(OH)_6 \cdot xH_2O$, ZHS).[2,3] On the other hand, the water-rich solvation structure with sluggish

desolvation kinetics and the uneven electric field distribution of corroded Zn metal lead to the inhomogeneous Zn^{2+} flux and deposition on Zn anode interface, which causes the rampant dendrite growth.[4,5] These severe interfacial issues associated with Zn anode result in the low Coulombic efficiency (CE), fast capacity degradation, and limited cycle life of AZIBs, especially when operating under high current density and high depth discharge, which limits their further commercialization.[6,7] Therefore, the cooperative regulation of solvation and interface is highly important to obtain high-performance batteries.[8,9]

Several strategies have been proposed to address the persistent challenges posed by interfacial phenomena, including structural design, electrolyte engineering, and surface coating.[10,11] Zhou et al.[12] have introduced polydopamine (PDA) layer-coated metallic zinc with dual effects of fast desolvation and ion confinement for high-performance AZIBs. Of these, electrolyte engineering offers a particularly straightforward and cost-effective approach, readily integrable into existing production lines without requiring additional capital investment.[13–15] By tailoring the Zn^{2+} solvation structure and/or regulating the Zn anode interface, electrolyte engineering can effectively suppress parasitic reactions and dendrite formation, thereby extending the cycle life of AZIBs.[16,17] By increasing zinc salt concentration or introducing high donor-number organic cosolvents such as methanol, dimethyl sulfoxide, and carbonate, these organic molecules and anion of zinc salt enter into Zn^{2+} solvation shell, which results in the solvation transformation from water-rich structure to water-poor structure.[18] Alternatively, some highly polar additives such as biomolecule, polymer, zwitterion, or quaternary ammonium salt can guide uniform

[*] M. Su, J. Yan, S. Liu, Prof. X. Wang
Institute of Carbon Neurtrality, Zhejiang Wanli University, Ningbo 315100, China
E-mail: wangx@zwu.edu.cn
          wangxin@scnu.edu.cn

M. Su, J. Yan, S. Liu, Prof. X. Wang
South China Academy of Advanced Optoelectronics, South China Normal University, Guangzhou 510006, China

Prof. H. Dou, M. Xu, C. Liu, Prof. Z. Chen
Power Battery and Systems Research Center, State Key Laboratory of Catalysis, Dalian Institute of Chemical Physics, Chinese Academy of Science Dalian, Dalian 116023, China
E-mail: zwchen@dicp.ac.cn
          haozhen@dicp.ac.cn

🖥 Additional supporting information can be found online in the Supporting Information section

Zn^{2+} nucleation and deposition via the mechanism of preferential adsorption, electrostatic shielding, or formation a protective layer on the Zn anode interface.[18,19] Despite the dramatic advancements, the current research primarily focuses on single-site additives, and single-site solvation coordination and single-site interface adsorption result in the limited reduction of thermodynamically active water, exposing the zinc anode to the risks of side reactions and dendrite growth.[20,21] Moreover, the regulation effectiveness highly depends on the high additive concentration, which potentially sacrifices the advantages of aqueous electrolytes and fast interface kinetics.[22] Very recently, some pioneering works have reported that trace additives with multiple solvation sites or multiple adsorption sites can significantly boost reversibility of Zn anode.[23] Zhou et al.[24] have demonstrated that two carbonyl groups of N-acetyl-ε-caprolactam can serve as dual solvation sites to coordinate with Zn^{2+}, which means one additive molecule can replace two water molecules within solvation shell. Cao et al.[25,26] have reported the utilization of straight-chain molecules with dual adsorption sites for achieving the comprehensive interface coverage. However, the development of multisite additives is still in its infancy, and designing multisite additives that simultaneously maximize the solvation and interface regulation remains a significant challenge.[27] The structure-performance of additives needs to be established urgently, particularly regarding the molecular spatial configurations and their dynamic evolution.[28–30]

In this contribution, dynamic configuration reconstruction mechanism of multifunctional-group molecules (MGMs) is proposed, which can maximize the cooperative regulation of Zn^{2+} solvation structure and interface via multisite coordination, thus significantly boosting the reversibility of Zn anode, especially at low concentrations of additives. A series of polyhydroxy additives with different functional-group number and chain length are selected as prototypes to unveil the structure–performance relationship of additives, including methanol (MeOH), ethanol (EtOH), ethylene glycol (EG), isopropanol (IPA), and glucose (DG), which demonstrates that the increase of functional groups and chain flexibility in MGMs contributes to boosting battery performance. As revealed by the combination of experiment and theoretical calculation, MGM exhibits the folded configuration and engages in multisite Zn^{2+} coordination in the solvation shell to replace 2–3 H_2O molecules, effectively minimizing the number of active water molecules. Moreover, MGM witnesses the configuration transition to straight-chain architecture from solvation structures to the electrode interface, which enables multisite parallel adsorption on Zn anode interface, thus creating a unique water-poor interface. The cooperative regulation of solvation and interface reconstructs the hydrogen-bond networks, accelerates desolvation kinetics, and steers (002)-facet-dominated Zn deposition, which suppresses parasitic reactions and dendrite growth. As a result, Zn//Zn symmetric cells can achieve long cycle life of 7000 h and can survive at low temperatures, and Zn//PANI full cell paired with polyaniline (PANI) exhibits a superior capacity retention of 72.5% after 5000 cycles at 5 A g^{-1}. The in-depth mechanism investigation of multisite additives sheds light on designing advanced additives for high-performance batteries via configuration tailoring and multi-functional group collaboration.

Results and Discussion

In aqueous electrolyte, AZIBs tended to experience serious side reactions and uncontrollable growth of dendritic Zn.[31] Those annoying problems were closely related to the existence of highly reactive water molecules. During battery cycling processes, solvated Zn-ions are prone to desolvating parts of the water molecules before reaching the surface of Zn-metal.[32,33] These desolvated highly reactive water molecules, combined with various free water molecules, severely corroded Zn-metal and accelerated the HER, inducing the formation of H_2 and ZHS as well as dendritic Zn (Figure 1a). Traditional single-site additive (SSA), such as methanol, modulates solvation structure and electrode interface through single active site, yet their inhibitory effect on zinc dendrites still fails to meet practical requirements (Figure 1b). MGMs like glucose retain the flexibility of molecular chains while coupling Zn^{2+} through multiple coordination sites, effectively reducing active water content. More importantly, these polyfunctional molecules enable molecular dynamic rearrangement, exhibiting linear chain structures at the electrode interface with multisite parallel adsorption. This configuration maximizes interfacial contact area to homogenize zinc deposition, thereby suppressing dendrite growth and side reactions (Figure 1c).

To probe the structure–performance correlations between molecular architectures and battery performance, this contribution systematically investigates methanol (MeOH), ethanol (EtOH), ethylene glycol (EG), isopropanol (IPA), and glucose (DG) as additives, representing a series of molecules with varying chain lengths and numbers of functional groups.[34,35] Electrostatic potential (ESP) mapping analysis was chosen to visualize the charge distribution of the additives (Figure 2a). It is found that with the extension of molecular chains and the increase in functional groups, molecular dimensions significantly expand while structural flexibility is simultaneously enhanced.[36,37] Concurrently, the multiple functional groups establish an enriched hydrogen-bonding network, enabling effective regulation of the electrolyte structure. The Zn//Zn symmetric batteries were assembled to evaluate the cycling stability of Zn-metals within different electrolytes at a current density of 0.5 mA cm^{-2} with a capacity of 0.5 mAh cm^{-2}. Experimental studies demonstrate that in a 0.1 M low-concentration system, battery cycling performance exhibits systematic improvement with increasing molecular carbon chain length and number of functional groups (Figure 2b). Notably, the MGM system achieves three orders of magnitude enhancement compared to monofunctional additives while maintaining consistent performance trends even at a higher concentration of 0.5 M (Figure 2c). This demonstrates that optimizing molecular chain length and functional group number effectively enhances overall battery performance.

The binding energy between the MGM molecule and the Zn^{2+} was calculated using density functional theory (DFT), elucidating the microscopic mechanism of the solvation
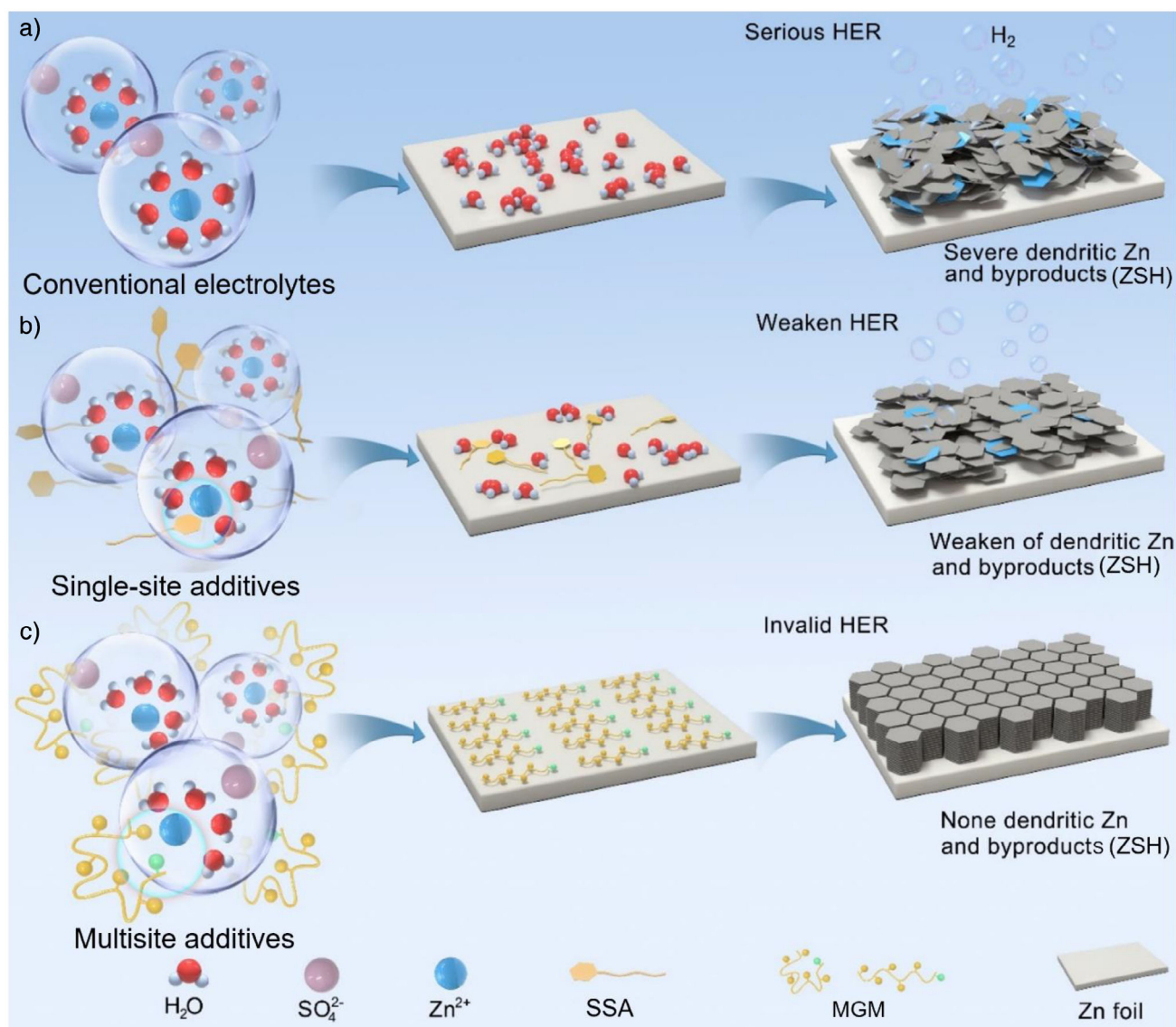
Figure 1. Design concept of multisite-coordinated regulation based on dynamic molecular engineering. a) Conventional electrolytes suffer from HER and dendrites. b) Single-site additives (CH₃OH) partially alleviate HER and dendrites through single-site regulation. c) Multisite additives (MGM) effectively suppress HER and dendrites via molecular dynamic rearrangement engineering.

structure reconstruction and interfacial adsorption process mediated by the MGM molecule.[38] DFT calculations reveal that the binding energy between MGM molecules and Zn^{2+} increases synchronously with the number of coordination sites, demonstrating MGM's critical role in solvation structure regulation (Figure S1a,b). When simultaneous coordination occurs at C1/C2/C5/C6 sites, the system achieves maximum binding energy, confirming that MGM adopts a folded configuration to reach optimal coordination states (Figure 2d). This coordination process displaces 2–3 water molecules from the Zn^{2+} solvation shell, effectively reducing free water content in the electrolyte and thereby suppressing HER and metal corrosion. Linear sweep voltammetry (LSV) measurements provide experimental validation for this mechanism (Figure 2e). DFT calculations further elucidate the interfacial regulation mechanism of MGM at electrodes (Figures 2f and

S2). The results demonstrate that the adsorption strength of MGM on the Zn (002) crystal plane is closely related to its molecular configuration orientation, with MGM preferentially aligning parallel to the electrode surface in a linear configuration to form an ordered protective layer. When C3/C4 sites establish a synergistic adsorption configuration, the interfacial adsorption energy reaches its peak value. Scanning electron microscopy (SEM) image of Zn anode after 30 cycles in MGM electrolyte displays dense and uniform deposition morphologies, indicating selective adsorption of MGM effectively regulates zinc deposition behavior (Figure 2g). The proposed "folded coordination-parallel adsorption" dynamic configuration transition strategy achieves remarkable battery performance enhancement through simultaneous optimization of solvation structures (HER suppression) and interfacial deposition behavior (dendrite inhibition). This synergistic
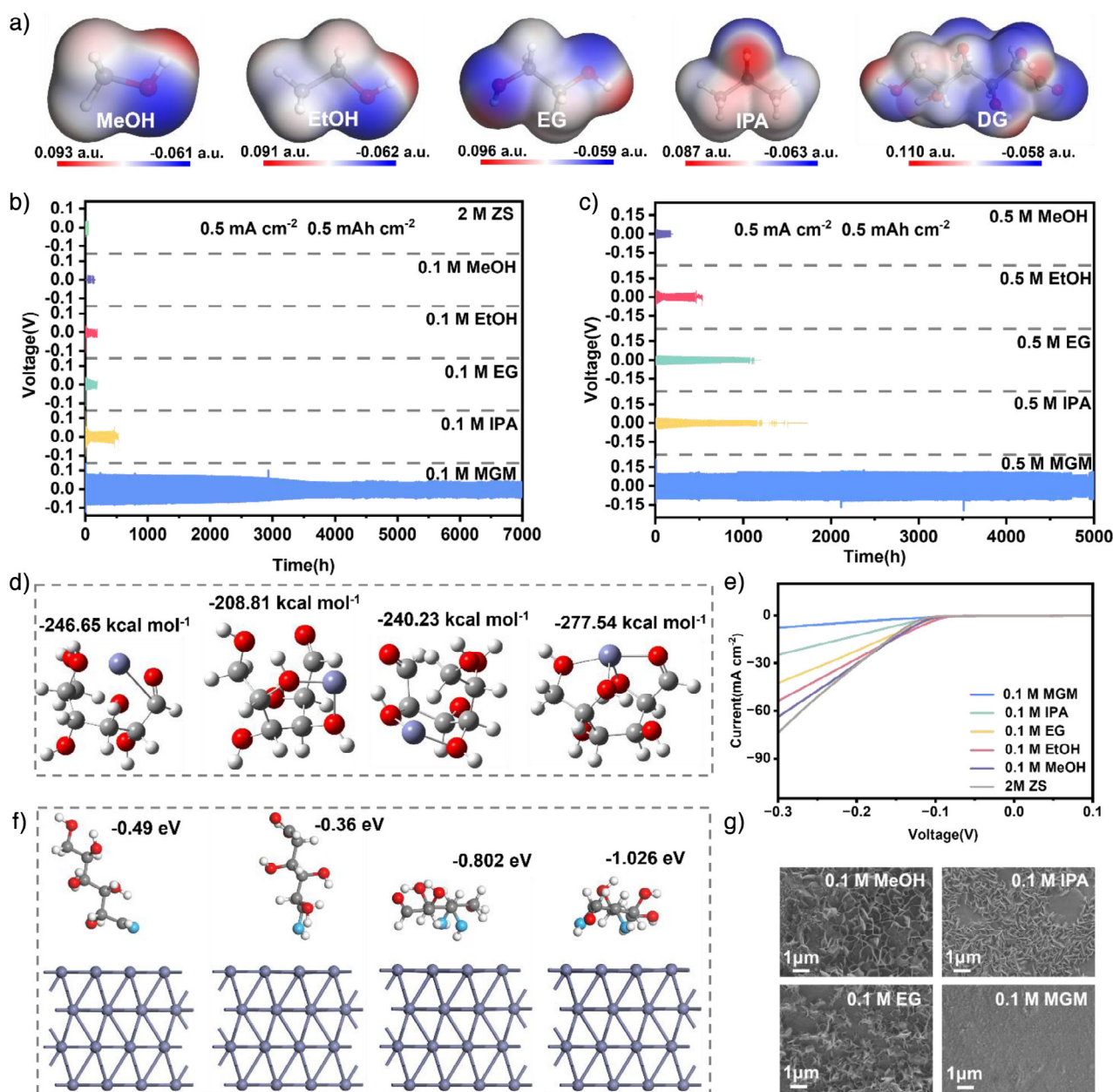
Figure 2. Mechanism of molecular dynamic reconstruction. a) Electrostatic potential (ESP) mapping of the solvated structures of pristine DG and a series of alcohol molecules. b) and c) Cycling performance of Zn//Zn symmetric cells in five electrolytes at 0.5 mA cm^{-2} and 0.5 mA h cm^{-2}. d) The binding energies of different sites between Zn^{2+} and MGM. e) LSV curves of Zn metal worked with different electrolytes. f) The adsorption energy of different MGM sites on the Zn (002) plane. g) SEM images of Zn anodes after 30 cycles in different electrolytes at 0.5 mA cm^{-2} and 0.5 mA h cm^{-2}.

effect originates from MGM's unique molecular architecture, where multiple functional groups independently mediate solvation structure reconstruction and interfacial deposition regulation, establishing a dual protection mechanism.[39]

This contribution systematically interprets the chemical effects of MGM from the perspective of molecular interactions and further analyzes the regulatory mechanism of MGM on the electrolyte system. Experimental results demonstrate that MGM exhibits excellent solubility in 2 M ZnSO$_4$ electrolyte, maintaining a clear and transparent solution (Figure S3). However, ionic conductivity tests reveal a gradual decline in electrolyte conductivity with increasing

MGM concentration (Figure S4), attributed to the "steric hindrance effect" of MGM molecules enhancing solution viscosity and impeding ion migration.[40] Fourier transform infrared (FT-IR) provides insights into solute coordination environments (Figure 3a). The characteristic C—O peaks of MGM (1078, 1031.5, and 989.5 cm^{-1}) exhibit high-wavenumber shifts, confirming hydroxyl oxygen coordination with Zn^{2+} to form Zn—O bonds, thereby redistributing C—O bond electron cloud density.[41,42] The SO$_4^{2-}$ characteristic peak (1085.7 cm^{-1}) displays a significant blue shift, indicating MGM weakens Zn^{2+}—SO$_4^{2-}$ electrostatic coupling through competitive coordination while forming novel
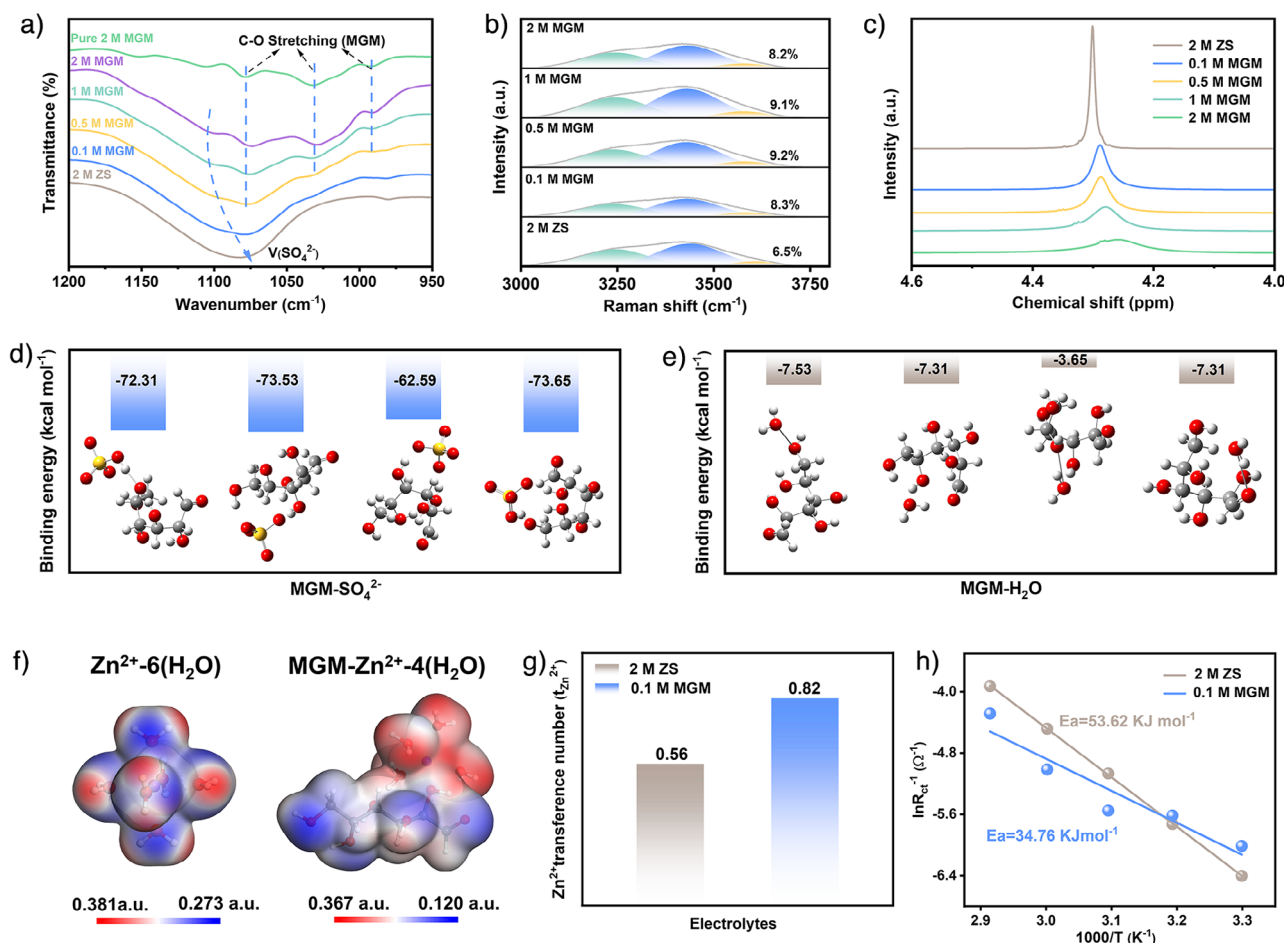
Figure 3. Regulating effect on Zn^{2+} solvation structure. a) FT-IR spectra and b) Raman spectra of 2 M $ZnSO_4$ (ZS) electrolytes with different concentrations of MGM. c) ^1H NMR spectra of different electrolytes. d) and e) Binding energies of MGM with SO_4^{2-} and MGM with H_2O. f) Electrostatic potential (ESP) mapping of the solvated structures of pristine Zn^{2+}–6(H_2O) and MGM-Zn^{2+}–4(H_2O). g) Calculated Zn^{2+} transfer numbers. h) Arrhenius curves and comparison of the activation energies.

MGM-SO_4^{2-} complexes.[43,44] The characteristic shift of the O—H stretching vibration peak toward 3500 cm^{-1} confirms that MGM molecules enter the Zn^{2+} solvation shell, displacing a portion of active water molecules (Figure S5). This solvation structure adjustment disrupts the original strong hydrogen-bonding network of water molecules while reconstructing a new hydrogen-bonding network mediated by the hydroxyl group of MGM. Raman spectroscopy (3000–3800 cm^{-1}) analysis further reveals a significant reduction in the intensity of the strong hydrogen-bond characteristic peak (~3450 cm^{-1}) in the MGM system, quantitatively verifying the weakening of hydrogen-bond interactions between water molecules (Figure 3b). The downfield shift of H_2O proton signal in ^1H nuclear magnetic resonance (NMR) provides additional evidence for the structural reorganization of the hydrogen-bond network.[45,46] Collectively, these results demonstrate that MGM effectively reduces active water content by reconstructing the solvation hydrogen-bond environment (Figure 3c). Temperature-dependent ^1H NMR studies reveal MGM-Zn^{2+} solvation effects on hydrogen bonds: as temperature decreases, H_2O peaks shift toward lower fields, explaining the observed freezing-point depres-

sion (Figure S6). Notably, all MGM-containing electrolytes demonstrate complete non-flammability in ignition tests (Figure S7), highlighting intrinsic safety advantages. DFT calculations reveal MGM's regulatory mechanism on electrolyte structure (Figure 3d–g). The strong interaction between MGM and SO_4^{2-} weakens the Zn^{2+}–SO_4^{2-} interaction, demonstrating that MGM effectively inhibits ion aggregation and promotes uniform Zn^{2+} distribution, thereby enhancing the Zn^{2+} transference number.[47] Simultaneously, the strong interaction between MGM and H_2O molecules weakens the Zn^{2+}–H_2O interaction, reducing water molecule activity and lowering the Zn^{2+} desolvation energy barrier. During solvation, MGM incorporates into the Zn^{2+} solvation shell to form MGM-Zn^{2+}–4(H_2O) hybrid complex. Compared with the Zn^{2+}–6(H_2O) system, this conformational transition significantly reduces the Zn^{2+} ESP, markedly weakening interionic repulsion.[48,49] Electrochemical tests confirm that MGM-containing symmetric cells exhibit a high Zn^{2+} transference number of 0.82 (Figures 3i and S8), and Arrhenius fitting reveals an activation energy of 34.76 kJ mol^{-1}, indicating significantly improved desolvation kinetics (Figures 3j and S9). These results demonstrate MGM's critical role in

Angew. Chem. Int. Ed. **2025**, 64, e202511685 (5 of 12)
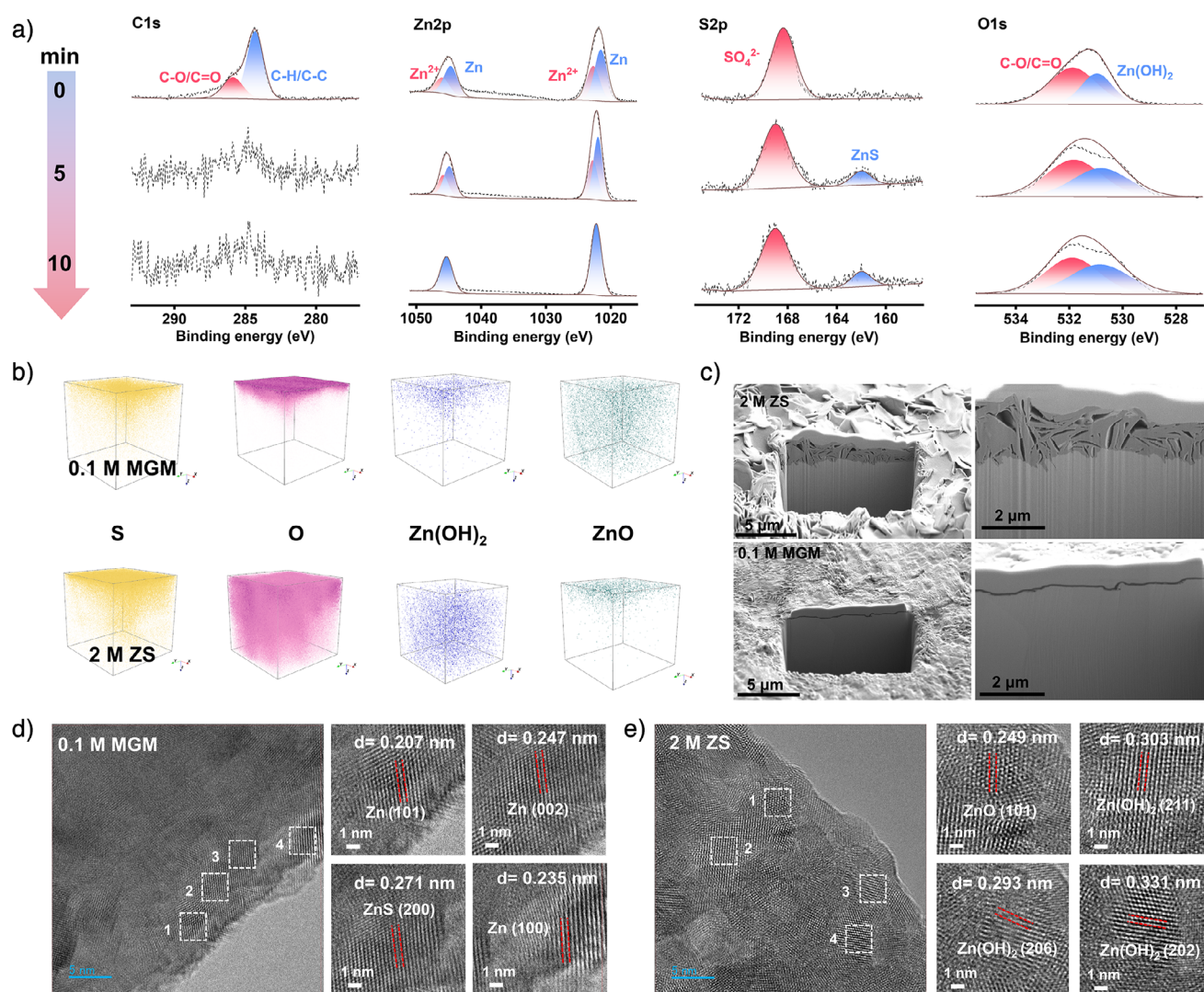
© 2025 Wiley-VCH GmbH

Figure 4. The morphology and chemical composition of the zinc anode surface. a) XPS spectra of Zn anode after 30 cycles in MGM electrolyte with in-depth profiles at Ar$^+$ sputtering times of 0, 300, and 600 s (from top to bottom): Zn 2p, S 2p, O 1s, and C 1s. b) 3D views of element distribution in the sputtering volume of TOF-SIMS for ZS and MGM electrolytes. c) Cross-sectional morphology of Zn anode captured by FIB after 30 cycles in ZS and MGM electrolytes. d) HR-TEM image of Zn anode after galvanostatic charging at 1 mA cm^{-2} for 10 min in MGM electrolyte. e) HR-TEM image of Zn anode after galvanostatic charging at 1 mA cm^{-2} for 10 min in ZS electrolyte.

Zn^{2+} desolvation and deposition processes. The interfacial chemistry of Zn anode after 30 cycles in ZS and MGM was characterized using X-ray photoelectron spectroscopy (XPS), time-of-flight secondary ion mass spectrometry (TOF-SIMS), transmission electron microscopy (TEM), and focused ion beam scanning electron microscopy (FIB-SEM). XPS spectra reveal distinct interfacial chemical reactions between MGM and ZS electrolytes (Figures 4a and S10). MGM exhibits stronger Zn signals, where the higher Zn content in the MGM Zn 2p spectrum confirms a uniform deposition layer. The C 1s spectrum demonstrates that its C−C/C−H and C−O components originate from MGM. The O 1s spectrum displays oxygen signals from $ZnCO_3$ and C=O/C−O, while the Zn (OH)$_2$ signal is negligible compared to ZS, indicating suppressed side reactions. Additionally, the S 2p spectrum shows SO_4^{2-} and ZnS derived from SO_4^{2-} decomposition, but with lower SO_4^{2-} content.[50] In contrast, ZS exhibits

higher Zn^{2+} content in the Zn 2p spectrum due to severe side reactions. The prominent Zn (OH)$_2$ signal in the O 1s spectrum further confirms extensive side reactions in ZS. The S 2p spectrum reveals that SO_4^{2-} remains dominant, suggesting substantial by-product formation. Consequently, a uniform and dense deposition layer form in MGM, enhancing interfacial stability. The elemental distribution and spatial structure of the deposition layer were further analyzed by TOF-SIMS (Figure 4b). The cycled MGM Zn anode surface shows homogeneous elemental distribution. In contrast, the ZS zinc anode exhibits distinct elemental gradients and defects, particularly highly inhomogeneous O and S distributions and abundant Zn (OH)$_2$ by-products, which hinder uniform zinc deposition.[51] FIB-SEM cross-sectional images (Figure 4c) and SEM cross-sectional views confirm loose and irregular zinc deposition in ZS, while MGM forms a uniform and compact deposition layer.[52]

HR-TEM further corroborates this (Figure 4d,e). The MGM-formed zinc anode surface primarily consists of metallic Zn, effectively suppressing interfacial water activity and mitigating HER and side reactions. In contrast, the ZS zinc anode surface is predominantly covered by ZnO and Zn(OH)$_2$, with structural instability being confirmed by the XPS results. Metals inherently undergo corrosion reactions upon contact with water, while the addition of MGM strongly inhibits side reactions, facilitating the formation of a uniform and dense surface.[53] Immersion tests conclusively verify the protective effect of MGM (Figures S11–S13).

To visualize Zn nucleation and deposition processes, in situ optical microscopy was employed to investigate the influence of the MGM on Zn deposition behavior.[54,55] In ZS at 5 mA cm^{-2}, uneven nucleation sites and protrusions (triggering "tip effects") emerged within just 5 min, followed by complete coverage of the anode with irregular Zn dendrites after 20 min. In stark contrast, the MGM maintained a flat and uniform electrode surface throughout the plating process.[56,57] These observations robustly validate MGM's efficacy in regulating Zn^{2+} deposition behavior to enhance anode reversibility, with corresponding in situ optical micrographs providing compelling visual evidence (Figures 5a and S14). To probe the intrinsic mechanisms underlying MGM-mediated Zn deposition and nucleation, SEM was utilized to characterize Zn anodes charged for 5, 15, and 30 min at 5 mA (Figure 5b). Zn anode in MGM-containing electrolytes develop regular and uniform Zn deposition nuclei dominated by horizontal growth and ordered layered deposition, favoring subsequent homogeneous Zn plating. Conversely, ZS produces irregular and protruding bulk nuclei on Zn anode, creating unfavorable conditions for uniform deposition—a finding further corroborated by in situ electrochemical atomic force microscopy (AFM) (Figure 5c). Cyclic voltammetry (CV), analyzed via nucleation overpotential (NOP) values, serves as another effective method to evaluate Zn deposition nucleation behavior. A higher NOP indicates stronger nucleation driving force, promoting the formation of fine-grained deposits with preferred crystallographic orientation.[58,59] The NOP for Zn deposition in MGM is 18.7 mV higher than in ZS, demonstrating that MGM enhances nucleation kinetics by reconstructing the solvation shell through bent coordination, thereby reducing desolvation activation energy (Figure 5d). The "spatial effect" reflects Zn^{2+} plating kinetics, where Zn^{2+} deposition predominantly follows 3D diffusion rather than 2D surface diffusion.[60] Chronoamperometry (CA) curves reveal that the ZS system exhibits continuously increasing current density beyond 300 s (dominated by prolonged 2D diffusion), whereas MGM transitions to stable 3D diffusion within 50 s.[61] This confirms that the planar adsorption layer restricts Zn^{2+} lateral migration, promoting 3D homogeneous deposition (Figure 5e).

A systematic investigation of the deposition behavior of Zn anodes in ZS and MGM electrolytes reveals the directional regulation effect of MGM on Zn deposition morphology. SEM analysis (Figures 6a and S15) demonstrates that in the ZS electrolyte, disordered vertically aligned dendrites emerge on the Zn anode after just 10 cycles. After 100 cycles, the dendritic size increases significantly,

accompanied by microcrack formation, which accelerates active material exfoliation and battery failure.[62,63] In stark contrast, Zn anode in the MGM system exhibits unique self-healing deposition characteristics—forming a dense lamellar structure after 10 cycles and maintaining intact layered morphology even after 100 cycles.[64] This excellent stability can be attributed to the effective suppression of side reactions by the MGM electrolyte. Linear sweep voltammetry (LSV) test results demonstrate that compared to the ZS electrolyte, the MGM electrolyte exhibits more negative overpotentials, confirming the effective inhibition of the hydrogen evolution reaction (HER) in the system due to the absence of thermodynamically active water molecules. Simultaneously, MGM significantly suppresses the oxygen evolution reaction (OER), as evidenced by the increased OER overpotential. To verify the universality of the MGM additive, comparative tests were conducted in a Na$_2$SO$_4$ neutral electrolyte system, where MGM still demonstrated its unique advantages. Meanwhile, the MGM enables the corrosion current density of the Zn electrode to decrease to 0.39 mA cm^{-2} (Figure S16), demonstrating that the Zn anode exhibits enhanced corrosion resistance under the unique molecular effect of MGM, leading to the formation of a uniform and dense Zn deposition layer. As further confirmed by 3D surface profilometry (Figure 6b and S17). The evolution of Zn dendrites is governed by the electrochemical behavior at the metal/electrolyte interface, where the crystallographic orientation of crystal planes plays a decisive role in deposition kinetics. DFT calculations elucidate the crystal plane-selective adsorption mechanism of MGM: the adsorption energy of MGM on the Zn (002) plane is significantly lower than that on Zn (100) and Zn (101) planes, yet higher than that of H$_2$O, indicating MGM preferentially adsorbs onto the Zn (002) plane through strong interactions (Figures 6c and S18). Notably, MGM molecules adopt a planar spreading mode to cover the Zn (002) plane, forming a kinetic barrier that forces Zn^{2+} to diffuse toward (100)/(101) planes, thereby slowing Zn^{2+} deposition and growth along the (002) direction. According to Bravais law, the orientation of crystal planes largely depends on the ion deposition rates across different planes. The finally exposed plane typically exhibits the lowest growth rate, whereas rapidly growing planes gradually diminish. Consequently, the minimal deposition rate of Zn^{2+} on the Zn (002) surface facilitates the exposure of ordered lamellar structures. Systematic analysis of XRD patterns from Zn//Zn symmetric cells at various cycling stages (Figures 6d,e and S19) unveils the precise regulation of Zn deposition crystallographic orientation by the MGM additive. The Zn anode cycled in MGM electrolyte shows only weak ZHS-related peaks (intensity reduced significantly compared to ZS), confirming MGM effectively blocks hydrolysis side reactions. The $I_{(002)}/I_{(101)}$ intensity ratio of cycled Zn anode increases markedly from 1.63 to 2.53 in MGM, while decreasing to 1.44 in ZS, demonstrating MGM-induced preferential exposure of the (002) plane. In Zn//Cu half-cell experiments, XRD characterization (Figures 6f and S20) reveals pronounced orientation regulation by MGM; under 1 mA cm^{-2} and 5 mAh cm^{-2} conditions, the (002) diffraction intensity ratio ($I_{(002)}/I_{(100)} = 5.34$) in MGM is fivefold higher than in ZS
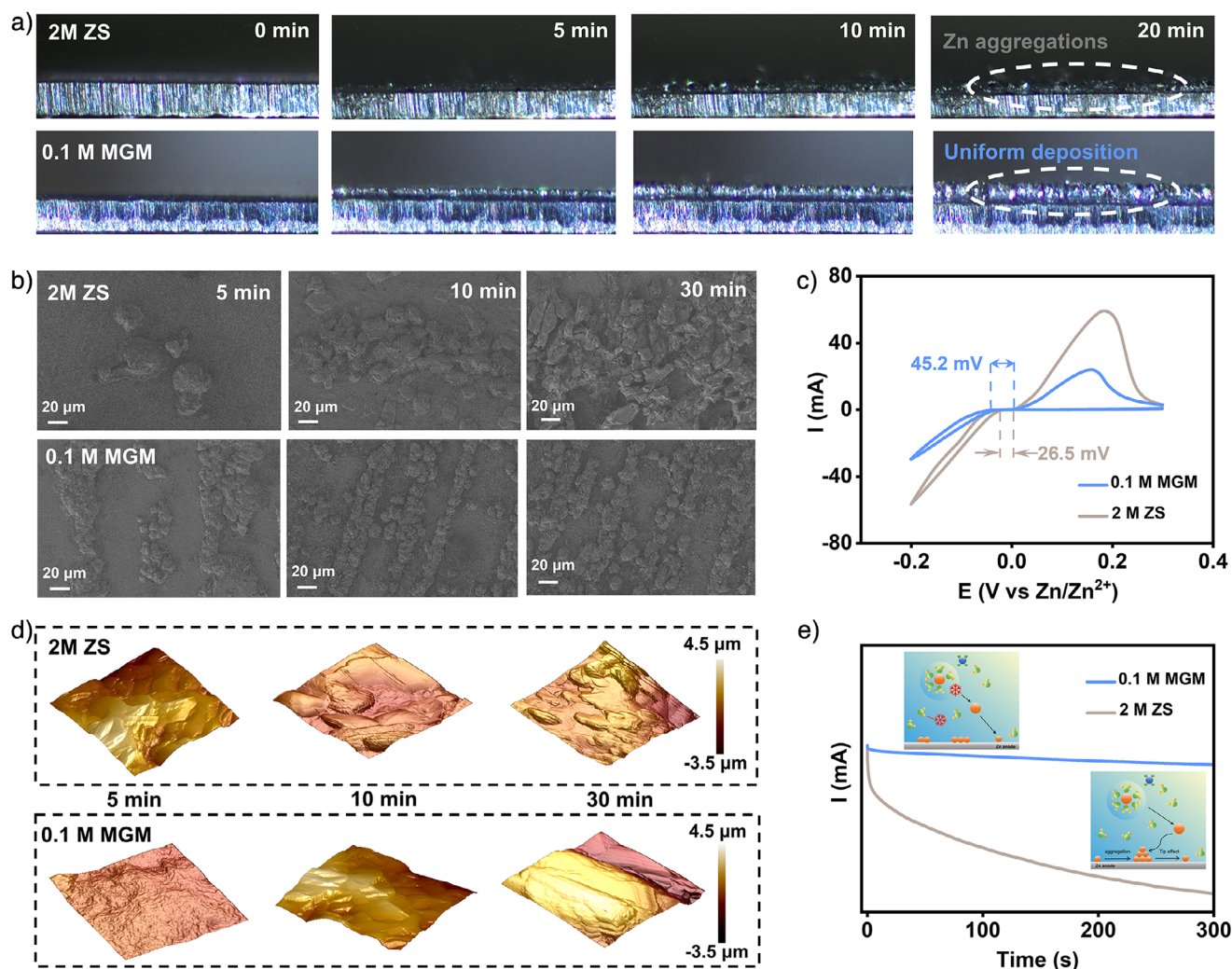
Figure 5. Nucleation behavior of zinc anodes. In situ optical microscopy of Zn deposition processes of Zn-metal assembled with a) ZS electrolyte and MGM electrolyte. b) SEM images and c) AFM images of Zn anode in 2 M ZS and MGM electrolytes after 10, 15, and 100 min charging at 5 mA cm^{-2}. d) CV curves of Zn//Ti cells in ZS and MGM electrolytes at 1 mV s^{-1}. e) CA curves for Zn electrode in ZS and MGM electrolytes, with insets showing the Zn^{2+} diffusion mode in different electrolytes.

(1.01), indicating MGM promotes (002)-oriented growth via planar adsorption templating. XRD spectra of Zn deposited at varied current densities consistently show enhanced (002) peak intensities, confirming the broad kinetic adaptability of MGM's orientation-control mechanism;[65,66] this facilitates the formation of a uniform and smooth zinc deposition layer. Meanwhile, electrochemical tests demonstrate that in the Zn//Cu cell system, the zinc nucleation overpotential in MGM electrolyte is approximately 42% lower than that in ZS electrolyte, with significantly improved deposition kinetics. This confirms the remarkable regulatory effect of MGM on the zinc deposition process (Figure S21).

The high reversibility of the Zn metal anode fully validates the superior functionality of MGM as an electrolyte additive. In symmetric cell configurations, the Zn//Zn cell containing 0.1 M MGM exhibits breakthrough cycling stability; under 0.5 mA cm^{-2} (0.5 mAh cm^{-2}) conditions, the cycle life exceeds 7000 h (Figure 7a), representing a 58-fold improvement over the ZS system (120 h). Even under practical operating conditions of 5 mA cm^{-2} (5 mAh cm^{-2}), stable operation for 3000 h is maintained (Figure 7b), and stable stripping-plating curves are observed at a high rate of 20 mA cm^{-2} (Figure 7c). Low-temperature performance tests further confirm that the MGM system can stably cycle for 1200 h at −10 °C, attributed to MGM reconstructing the Zn^{2+} solvation shell via bent solvation coordination, reducing desolvation activation energy by 35.8%, while simultaneously inhibiting interfacial water freezing (Figure 7d). Nearly 100% voltage recovery is achieved when the current density is restored from 5 mA cm^{-2} to 0.5 mA cm^{-2}, highlighting its exceptional kinetic adaptability (Figure 7e). For high-energy-density battery design, MGMeves stable cycling for 1200 h under conditions of a 20 μm ultrathin Zn anode and 85% depth of discharge (DOD) (Figure S22). Zn/Cu half-cell tests demonstrate a Coulombic efficiency (CE) exceeding 98.5% over 400 cycles (Figure S23), significantly outperforming the ZS system (CE drops to zero after 40 cycles). Additionally, stable charge–discharge profiles with acceptable polarization are achieved in
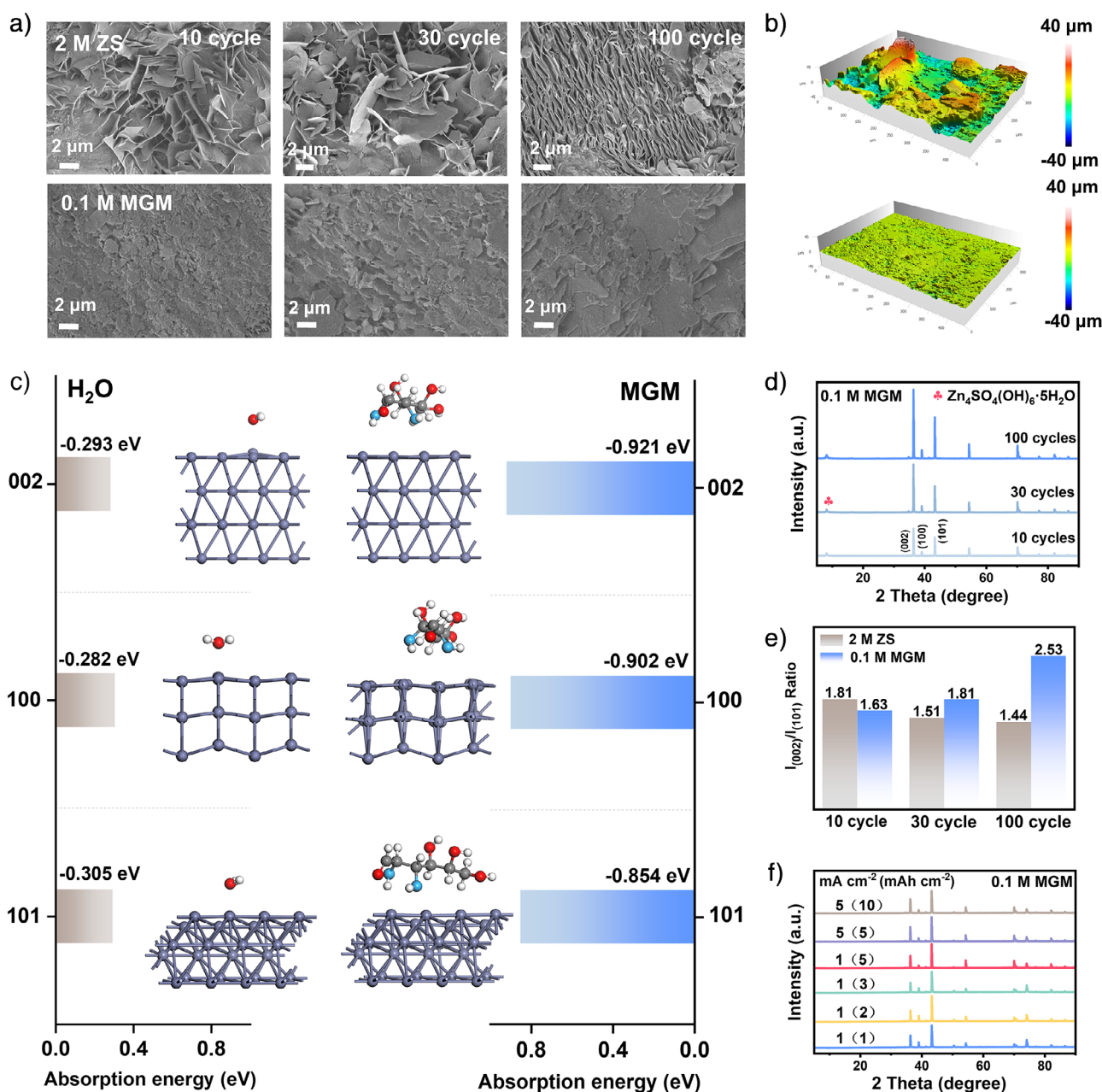
Angew. Chem. Int. Ed. **2025**, *64*, e202511685 (8 of 12)

© 2025 Wiley-VCH GmbH

Figure 6. Morphological evolution and crystallographic orientation of Zn deposition. a) SEM images of Zn anodes cycled in ZS and MGM electrolytes for 10, 30, and 100 cycles. b) 3D reconstructed LSCM images. c) Comparison of adsorption energies of MGM molecules and H_2O on different Zn crystalline planes. d) and e) XRD patterns of Zn anodes after 10, 30, and 100 cycles in MGM. And the corresponding Zn (002)/Zn (100) intensity ratios of different crystalline planes of cycled Zn metal from Zn//Zn. f) XRD patterns of Zn deposited on Cu at various current densities and deposition times in MGM electrolyte.

MGM-containing electrolytes (Figure S24). The practical potential of the MGM electrolyte is systematically evaluated using a Zn//PANI full-cell system.[67,68] Electrochemical behavior of PANI in MGM was understood by CV curves (Figure S25). CV curves exhibited two sets of reversible redox peaks and overlapped well in two cycles with no significant decrease in peak current, indicating the high stability and reversibility of PANI cathode in the MGM. At a current density of 1 A g^{-1} (Figure 7f), the full-cell with ZS electrolyte suffers rapid capacity decay and

failure after 600 cycles, whereas the MGM electrolyte demonstrates exceptional cycling stability: a capacity of 160.5 mAh g^{-1} (72% retention) is maintained after 1000 cycles, with highly reversible charge-discharge profiles (Figure 7g). Rate capability tests (Figure 7h) further confirm MGM's kinetic advantages: Specific capacities remain stable between 195 and 125 mAh g^{-1} across a wide current density range of 0.5–5 A g^{-1}. When the current density is restored to 0.5 A g^{-1}, the capacity rebounds to 195 mAh g^{-1} (recovery rate >98%), indicating significantly optimized interfacial
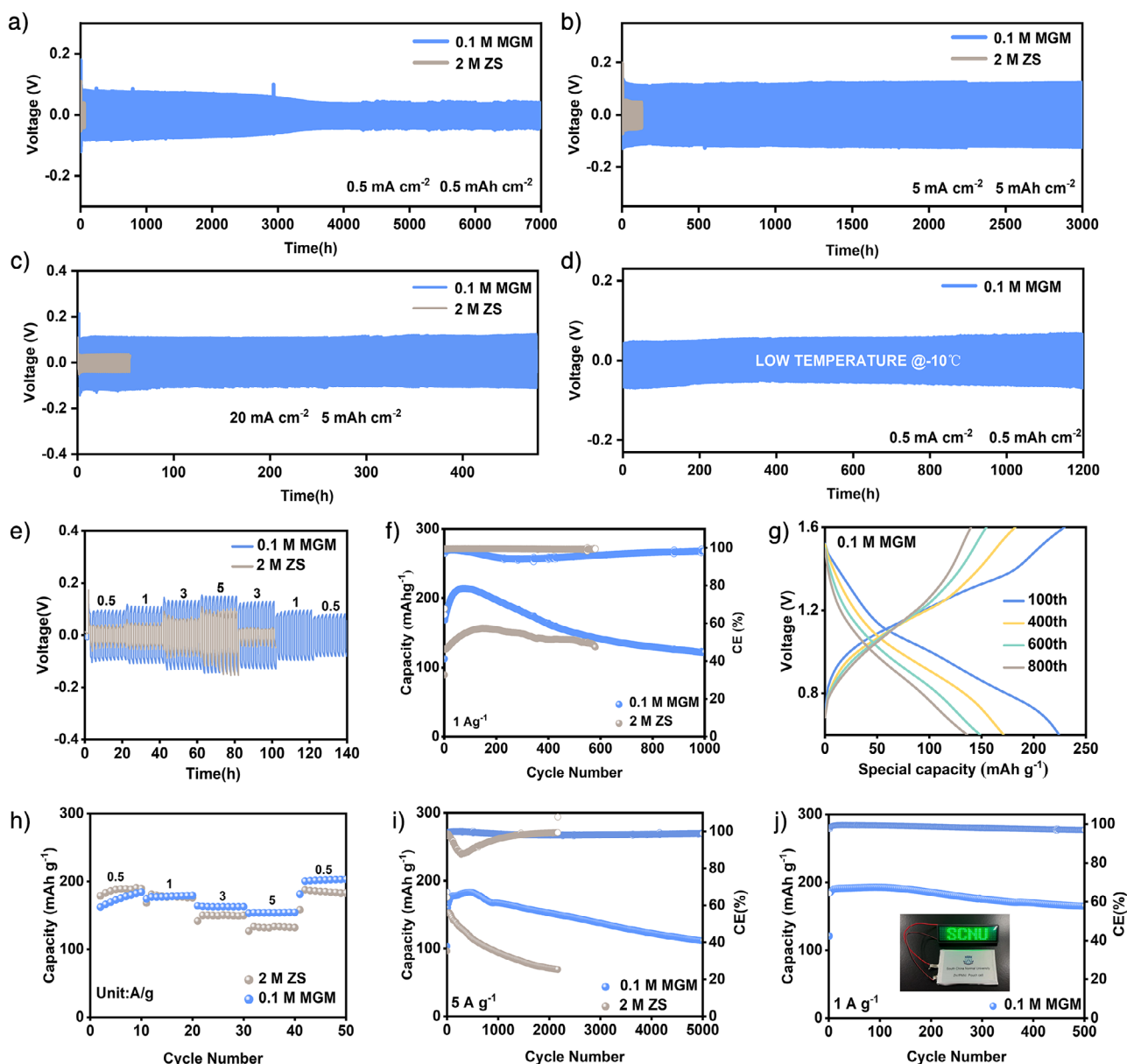
Figure 7. Electrochemical performance of AZIBs. a)–c) Cycling performance of Zn//Zn symmetric batteries based on ZS and MGM electrolytes under different currents and capacities (0.5 mA cm^{-2} at 0.5 mAh cm^{-2}, 5 mA cm^{-2} at 5 mAh cm^{-2}, 20 mA cm^{-2} at 5 mAh cm^{-2}). d) Cycling performance of Zn//Zn symmetric batteries based on ZS and MGM electrolytes under 0.5 mA cm^{-2} and 0.5 mAh cm^{-2} at −10 °C. e) Rate performance of the Zn//Zn symmetric batteries. f) and g) Voltage-capacity curves and cycling performance of the Zn//PANI batteries based on ZS electrolyte and MGM electrolyte at a current density of 1 A g^{-1}. h) Rate performance of the Zn//PANI batteries. i) Long-term stability of Zn//PANI batteries in different electrolytes at a current density of 5 A g^{-1}. j) Cycle performance of the Zn//PANI pouch cell based on MGM electrolyte.

reaction kinetics. At a high current density of 5 A g^{-1}, the MGM-based full cell retains a specific capacity of 210.6 mA h g^{-1} after 5000 cycles (68.5% capacity retention) with near-100% CE (Figure 7i). This performance enhancement is attributed to MGM's molecular-level interfacial regulation mechanism.[54,69] Notably, the MGM-containing electrolyte also performs exceptionally well in pouch cells. After 500 cycles at 1 A g^{-1}, the pouch cell maintains nearly 100% capacity retention with a reversible capacity of 180 mAh g^{-1}. The pouch cell can also stably power battery-powered devices (Figures 7g and S26), demonstrating the feasibility of MGM

for commercial applications in low-cost, high-safety zinc-ion batteries.[70]

Conclusions

In summary, a dynamic configuration reconstruction mechanism that orchestrates the multisite regulation of solvation and interface is unveiled by utilizing a series of polyhydroxy additive prototypes, demonstrating that the increase of functional groups and chain flexibility in MGMs contributes to

boosting battery performance. MGM with folded configuration engages in multisite Zn^{2+} coordination in solvation shell, effectively minimizing active H_2O molecules to suppress parasitic reactions, while its configuration transition to straight-chain architecture enables multisite parallel adsorption on Zn anode interface, thus accelerating desolvation kinetics and steering (002)-facet-dominated Zn deposition. Remarkably, Zn//Zn cells achieve long cycle life of 7000 h and subzero-temperature operation, and Zn//PANI pouch cell fully maintains nearly 100% capacity retention after 500 cycles. This study opens a fascinating avenue for developing high-performance batteries via dynamic additive engineering.

Acknowledgements

Conflict of Interests

The authors declare no conflict of interest.

Data Availability Statement

The data that support the findings of this study are available from the corresponding author upon reasonable request.

Keywords: Aqueous zinc-ion batteries · Dendrite-free deposition · Desolvation kinetics · Multifunctional-group molecules

[1] W. Yuan, X. Nie, G. Ma, M. Liu, Y. Wang, S. Shen, N. Zhang, *Angew. Chem. Int. Ed.* **2023**, *62*, e202218386.

[2] H. Wang, A. Zhou, X. Hu, Z. Song, B. Zhang, S. Gao, Y. Huang, Y. Cui, Y. Cui, L. Li, F. Wu, R. Chen, *Adv. Mater.* **2024**, *36*, 2407145.

[3] H. Y. Li, Y. Ren, Y. Zhu, J. M. Tian, X. Y. Sun, C. C. Sheng, P. He, S. H. Guo, H. S. Zhou, *Angew. Chem. Int. Ed.* **2023**, *62*, e202310143.

[4] X. Wang, W. Zhou, L. Wang, Y. Zhang, S. Li, X. Li, Z. Zhao, T. Zhang, H. Jin, X. Song, P. Liang, B. Zhang, D. Zhao, D. Chao, *Adv. Mater.* **2025**, *37*, 2501049.

[5] C. X. Zhao, L. G. Yu, J. N. Liu, J. Wang, N. Yao, X. Y. Li, X. Chen, B. Q. Li, Q. Zhang, *Angew. Chem. Int. Ed.* **2022**, *61*, e202208042.

[6] H. Ren, S. Li, L. Xu, L. Wang, X. Liu, L. Wang, Y. Liu, L. Zhang, H. Zhang, Y. Gong, C. Lv, D. Chen, J. Wang, Q. Lv, Y. Li, H. Liu, D. Wang, T. Cheng, B. Wang, D. Chao, S. Dou, *Angew. Chem. Int. Ed.* **2025**, *64*, e202423302.

[7] L. He, C. Lin, L. Zeng, F. Xiao, H. Lin, P. Xiong, Q. Qian, Q. Chen, Z. Yan, J. Chen, *Angew. Chem. Int. Ed.* **2024**, *64*, e202415221.

[8] Z. Hao, Y. Zhang, Y. Lu, J. Hou, X. Liu, Z. Yan, J. Chen, *Adv. Funct. Mater.* **2024**, *34*, 2315726.

[9] D. M. Xu, Z. Wang, C. J. Liu, H. Y. Li, F. Ouyang, B. Q. Chen, W. H. Li, X. T. Ren, L. S. Bai, Z. Chang, A. Q. Pan, H. S. Zhou, *Adv. Mater.* **2024**, *36*, 2403765.

[10] Z. Wei, G. Qu, Z. Huang, Y. Wang, D. Li, X. Yang, S. Zhang, A. Chen, Y. Wang, H. Hong, Q. Li, C. Zhi, *Adv. Mater.* **2024**, *36*, 2414388.

[11] L. Miao, J. Zhang, Y. Lv, L. Gan, M. Liu, *Chem. – A Eur. J.* **2023**, *29*, e202203973.

[12] T. Wang, P. Wang, L. Pan, Z. He, L. Dai, L. Wang, S. Liu, S. C. Jun, B. Lu, S. Liang, J. Zhou, *Adv. Energy Mater.* **2022**, *13*, 2203523.

[13] L. Ma, Q. Li, Y. Ying, F. Ma, S. Chen, Y. Li, H. Huang, C. Zhi, *Adv. Mater.* **2021**, *33*, 2007406.

[14] S. Y. Gao, B. M. Li, H. Y. Tan, F. Xia, O. Dahunsi, W. Q. Xu, Y. Z. Liu, R. Y. Wang, Y. W. Cheng, *Adva. Mater.* **2022**, *34*, 2201510.

[15] R. Jia, C. J. Yin, B. Wang, L. Li, J. S. Hu, *Chem. Eng. J.* **2024**, *500*, 157587.

[16] P. Wang, T. C. Li, Y. Liu, C. Lin, Y. Cui, H. Song, B. Lu, S. Liang, H. Y. Yang, J. Zhou, *Angew. Chem. Int. Ed.* **2025**, *64*, e202422547.

[17] S. Zhang, H. Ao, J. Dong, D. Wang, C. Wang, X. Xu, Z. Hou, J. Yang, *Angew. Chem. Int. Ed.* **2024**, *64*, e202414702.

[18] G. Ma, W. Yuan, X. Li, T. Bi, L. Niu, Y. Wang, M. Liu, Y. Wang, Z. Shen, N. Zhang, *Adv. Mater.* **2024**, *36*, 2408287.

[19] K. Qiu, G. Ma, Y. Wang, M. Liu, M. Zhang, X. Li, X. Qu, W. Yuan, X. Nie, N. Zhang, *Adv. Funct. Mater.* **2024**, *34*, 2313358.

[20] Z. Shen, Y. Liu, Z. Li, Z. Tang, J. Pu, L. Luo, Y. Ji, J. Xie, Z. Shu, Y. Yao, N. Zhang, G. Hong, *Adv. Funct. Mater.* **2024**, *35*, 2406620.

[21] K. Wu, Y. Wang, Y. Wan, W. Gu, L. Zhang, X. Yang, S. Chou, H. K. Liu, S. X. Dou, C. Wu, *Adv. Funct. Mater.* **2024**, *35*, 2412027.

[22] Y. Zong, H. He, Y. Wang, M. Wu, X. Ren, Z. Bai, N. Wang, X. Ning, S. X. Dou, *Adv. Energy Mater.* **2023**, *13*, 2300403.

[23] L. Liu, X. Wang, Z. Hu, X. Wang, Q. Zheng, C. Han, J. Xu, X. Xu, H. K. Liu, S. X. Dou, W. Li, *Angew. Chem. Int. Ed.* **2024**, *63*, e202405209.

[24] D. Xu, X. Ren, H. Li, Y. Zhou, S. Chai, Y. Chen, H. Li, L. Bai, Z. Chang, A. Pan, H. Zhou, *Angew. Chem. Int. Ed.* **2024**, *63*, e202402833.

[25] F. Wu, J. Zhang, L. Ma, P. Ruan, Y. Chen, S. Meng, R. Yin, W. Shi, W. Liu, J. Zhou, X. Cao, *Angew. Chem. Int. Ed.* **2024**, *64*, e202421787.

[26] X. M. Yao, S. M. Chen, C. H. Wang, T. W. Chen, J. X. Li, S. D. Xue, Z. K. Deng, W. G. Zhao, B. W. Nan, Y. Q. Zhao, K. Yang, Y. L. Song, F. Pan, L. Y. Yang, X. L. Sun, *Adv. Energy Mater.* **2024**, *14*, 2303422.

[27] Y. Zhang, Y. Wang, X. Yang, H. Liu, K. Wu, L. Zhang, D. Chao, L. Lin, S.-X. Dou, C. Wu, *Energy Storage Mater.* **2025**, *78*, 104246.

[28] H. Dou, X. Wu, M. Xu, R. Feng, Q. Ma, D. Luo, K. Zong, X. Wang, Z. Chen, *Angew. Chem. Int. Ed.* **2024**, *63*, e202401974.

[29] J. Huang, Y. Zhong, H. Fu, Y. Zhao, S. Li, Y. Xie, H. Zhang, B. Lu, L. Chen, S. Liang, J. Zhou, *Adv. Mater.* **2024**, *36*, 2406257.

[30] X. Shi, Y. Zhong, Y. Yang, J. Zhou, X. Cao, S. Liang, *Angew. Chem. Int. Ed.* **2024**, *64*, e202414777.

[31] J. Zhu, Z. Tie, S. Bi, Z. Niu, *Angew. Chem. Int. Ed.* **2024**, *63*, e202403712.

[32] O. Licht, F. Breuer, K. Blümlein, S. Schwonbeck, D. Pallapies, R. Kellner, P. Wiedemeier, A. Bitsch, *EFSA Supporting Publications*, **2023**, *20*, 7893E.

[33] M. Yang, J. Zhu, S. Bi, R. Wang, H. Wang, F. Yue, Z. Niu, *Angew. Chem. Int. Ed.* **2024**, *63*, e202400337.

Angew. Chem. Int. Ed. **2025**, *64*, e202511685 (11 of 12)

© 2025 Wiley-VCH GmbH

[34] Y. Q. Zheng, P. X. Sun, X. Y. Zhang, N. W. Li, L. L. Wu, D. Y. Luan, X. T. Zhang, X. W. Lou, L. Yu, *Adv. Mater.* **2024**, *36*, 2405906.

[35] Y. Tian, Z. Pei, D. Luan, X. W. D. Lou, *Angew. Chem. Int. Ed.* **2025**, *64*, e202423454.

[36] J. Zhu, M. Yang, Y. Hu, M. Yao, J. Chen, Z. Niu, *Adv. Mater.* **2023**, *36*, 2304426.

[37] D. Q. Cai, H. Cheng, J.-L. Yang, H. Liu, T. Xiao, X. Liu, M. Chen, H. J. Fan, *Energy Environ. Sci.* **2024**, *17*, 8349–8359.

[38] C. J. Cui, D. L. Han, H. T. Lu, Z. G. Li, K. Y. Zhang, B. Zhang, X. X. Guo, R. Sun, X. L. Ye, J. C. Gao, Y. X. Liu, Y. Guo, R. W. Meng, C. G. Wei, L. C. Yin, F. Y. Kang, Z. Weng, Q. H. Yang, *Adv. Energy Mater.* **2023**, *13*, 2301466.

[39] Q. Zhang, P. Zhi, J. Zhang, S. Duan, X. Yao, S. Liu, Z. Sun, S. C. Jun, N. Zhao, L. Dai, L. Wang, X. Wu, Z. He, Q. Zhang, *Adv. Mater.* **2024**, *36*, 2313152.

[40] D. Tang, X. Y. Zhang, D. L. Han, C. J. Cui, Z. S. Han, L. Wang, Z. G. Li, B. Zhang, Y. X. Liu, Z. Weng, Q. H. Yang, *Adv. Mater.* **2024**, *36*, 2406071.

[41] S. Deng, Z. Tie, F. Yue, H. Cao, M. Yao, Z. Niu, *Angew. Chem. Int. Ed.* **2022**, *61*, e202115877.

[42] P. Sun, L. Ma, W. Zhou, M. Qiu, Z. Wang, D. Chao, W. Mai, *Angew. Chem. Int. Ed.* **2021**, *60*, 18247–18255.

[43] Y. Ding, X. Zhang, T. Wang, B. Lu, Z. Zeng, Y. Tang, J. Zhou, S. Liang, *Energy Storage Mater.* **2023**, *62*, 102949.

[44] Z. H. Sun, F. X. Bu, Y. Y. Zhang, W. H. Zhou, X. R. Li, X. Liu, H. R. Jin, S. X. Ding, T. S. Zhang, L. P. Wang, H. P. Li, W. Li, C. F. Zhang, D. Y. Zhao, Y. G. Wang, D. L. Chao, *Angew. Chem. Int. Ed.* **2024**, *63*, e202402987.

[45] J. Yan, E. H. Ang, Y. Yang, Y. Zhang, M. Ye, W. Du, C. C. Li, *Adv. Funct. Mater.* **2021**, *31*, 2010213.

[46] D. Wang, D. Lv, H. Peng, C. Wang, H. Liu, J. Yang, Y. Qian, *Angew. Chem. Int. Ed.* **2023**, *62*, e202310290.

[47] Z. Peng, X. Shen, B. Li, J. Cheng, Z. He, Z. Sun, B. Li, Z. Zhang, Z. Zhuang, X. Wu, L. Dai, L. Wang, G. He, Q. Zhang, *Prog. Mater. Sci.* **2025**, *152*, 101453.

[48] D. Wang, H. Liu, D. Lv, C. Wang, J. Yang, Y. Qian, *Adv. Mater.* **2022**, *35*, 2207908.

[49] J. Dong, L. Su, H. Peng, D. Wang, H. Zong, G. Wang, J. Yang, *Angew. Chem. Int. Ed.* **2024**, *63*, e202401441.

[50] X. Li, C. Cai, P. Hu, B. Zhang, P. Wu, H. Fan, Z. Chen, L. Zhou, L. Mai, H. J. Fan, *Adv. Mater.* **2024**, *36*, 2400184.

[51] S. L. Li, J. Shang, M. L. Li, M. W. Xu, F. B. Zeng, H. Yin, Y. B. Tang, C. P. Han, H. M. Cheng, *Adv. Mater.* **2023**, *35*, 2207115.

[52] H. Wu, J. N. Hao, S. J. Zhang, Y. L. Jiang, Y. L. Zhu, J. H. Liu, K. Davey, S. Z. Qiao, *J. Am. Chem. Soc.* **2024**, *146*, 16601–16608.

[53] H. Li, J. Hao, S. Z. Qiao, *Adv. Mater.* **2024**, *36*, 2411991.

[54] R. Z. Zhang, W. K. Pang, J. Vongsvivut, J. A. Yuwono, G. J. Li, Y. Lyu, Y. M. Fan, Y. L. Zhao, S. L. Zhang, J. F. Mao, Q. Cai, S. L. Liu, Z. P. Guo, *Energy Environ. Sci.* **2024**, *17*, 4569–4581.

[55] G. J. Li, L. Sun, S. L. Zhang, C. F. Zhang, H. Y. Jin, K. Davey, G. M. Liang, S. L. Liu, J. F. Mao, Z. P. Guo, *Adv. Funct. Mater.* **2024**, *34*, 2301291.

[56] X. Cai, X. Wang, Z. Bie, Z. Jiao, Y. Li, W. Yan, H. J. Fan, W. Song, *Adv. Mater.* **2023**, *36*, 2306734.

[57] T. Sun, Z. Yi, W. Zhang, Q. Nian, H. J. Fan, Z. Tao, *Adv. Funct. Mater.* **2023**, *33*, 2306675.

[58] T. Q. Wu, C. Hu, Q. Zhang, Z. F. Yang, G. H. Jin, Y. X. Li, Y. G. Tang, H. H. Li, H. Y. Wang, *Adv. Func. Mater.* **2024**, *34*, 2315716.

[59] F. F. Wang, W. B. Liang, X. Y. Liu, T. Y. Yin, Z. H. Chen, Z. J. Yan, F. B. Li, W. Liu, J. Lu, C. P. Yang, Q. H. Yang, *Adv. Energy Mater.* **2024**, *14*, 2400110.

[60] P. Liang, J. Li, Y. Dong, Z. Wang, G. Ding, K. Liu, L. Xue, F. Cheng, *Angew. Chem. Int. Ed.* **2024**, *64*, e202415853.

[61] D. Gupta, S. Liu, R. Zhang, Z. Guo, *Adv. Energy Mater.* **2025**, *15*, 2500171.

[62] L. Jin, G. S. Selopal, X. Liu, D. Benetti, F. Rosei, *Adv. Funct. Mater.* **2024**, *34*, 2405653.

[63] L. Yan, Q. Zhu, Y. E. Qi, J. Xu, Y. Peng, J. Shu, J. Ma, Y. G. Wang, *Angew. Chem. Int. Ed.* **2022**, *61*, e202211107.

[64] Y. Liu, L. Zhang, L. Liu, Q. Ma, R. Wang, P. Xiong, H. Li, S. Zhang, J. Hao, C. Zhang, *Adv. Mater.* **2025**, *37*, 2415979.

[65] F. F. Wang, J. P. Zhang, H. T. Lu, H. B. Zhu, Z. H. Chen, L. Wang, J. Y. Yu, C. H. You, W. H. Li, J. W. Song, Z. Weng, C. P. Yang, Q. H. Yang, *Nat. Commun.* **2023**, *14*, 4211.

[66] Y. Gao, Q. H. Cao, J. Pu, X. Zhao, G. W. Fu, J. P. Chen, Y. X. Wang, C. Guan, *Adv. Mater.* **2023**, *35*, 2207573.

[67] C. Y. Chang, S. L. Hu, T. T. Li, F. B. Zeng, D. Wang, S. D. Guo, M. W. Xu, G. J. Liang, Y. B. Tang, H. F. Li, C. P. Han, H. M. Cheng, *Energy Environ. Sci.* **2024**, *17*, 680–694.

[68] C. Wang, B. Chen, T. Wang, G. V. D. Silva, Z. Xu, G. X. Miao, Y. H. Huang, J. Fu, *Energy Environ. Sci.* **2024**, *17*, 5429–5439.

[69] Z. Liu, M. Xi, G. Li, Y. Huang, L. Mao, J. Xu, W. Wang, Z. Qi, J. Ding, S. Zhang, Z. Guo, *Adv. Mater.* **2024**, *37*, 2413677.

[70] Q. H. Cao, Y. Gao, J. Pu, X. Zhao, Y. X. Wang, J. P. Chen, C. Guan, *Nat. Commun.* **2023**, *14*, 641.

Angew. Chem. Int. Ed. **2025**, *64*, e202511685 (12 of 12)

© 2025 Wiley-VCH GmbH